ACS APPLIED MATERIALS & INTERFACES

Research Article

www.acsami.org

Lithium Storage Properties of Pristine and (Mg, Cu) Codoped $ZnFe_2O_4$ Nanoparticles

A. Shahul Hameed,[†] Hamed Bahiraei,[‡,§] M. V. Reddy,*[,∥,⊥] Morteza Zargar Shoushtari,[‡] Jagadese J. Vittal,[†] Chong Kim Ong,[∥] and B. V. R. Chowdari[∥]

[†]Department of Chemistry, National University of Singapore, Singapore 117543

[‡]Department of Physics, Shahid Chamran University, Ahvaz, Iran 6135713749

[§]Department of Physics, Malayer University, Malayer, Iran 6571995863

[∥]Department of Physics, National University of Singapore, Singapore 117542

[⊥]Department of Materials Science and Engineering, National University of Singapore, Singapore 117576

Supporting Information

ABSTRACT: $ZnFe_2O_4$ and $Mg_xCu_{0.2}Zn_{0.82-x}Fe_{1.98}O_4$ (where x = 0.20, 0.25, 0.30, 0.35, and 0.40) nanoparticles were synthesized by sol–gel assisted combustion method. X-ray diffraction (XRD), FTIR spectroscopy, Raman spectroscopy, scanning electron microscopy (SEM), transmission electron microscopy (TEM), and Brunauer–Emmett–Teller (BET) surface area studies were used to characterize the synthesized compounds. $ZnFe_2O_4$ and the doped compounds crystallize in *Fd*3*m* space group. The lattice parameter of $ZnFe_2O_4$ is calculated to be a = 8.448(3) Å, while the doped compounds show a slight decrease in the lattice parameter with an increase in the Mg content. The particle size of all the compositions are in the range of ∼50–80 nm, and the surface area of the compounds are in the range of 11–12 m^2 g^{-1}. Cyclic voltammetry (CV), galvanostatic cycling, and electrochemical impedance spectroscopy (EIS) studies were used to investigate the electrochemical properties of the different compositions. The as-synthesized samples at 600 °C show large-capacity fading, while the samples reheated at 800 °C show better cycling stability. $ZnFe_2O_4$ exhibits a high reversible capacity of 575 mAh g^{-1} after 60 cycles at a current density of 100 mA g^{-1}. $Mg_{0.2}Cu_{0.2}Zn_{0.62}Fe_{1.98}O_4$ shows a similar capacity of 576 mAh g^{-1} after 60 cycles with better capacity retention.

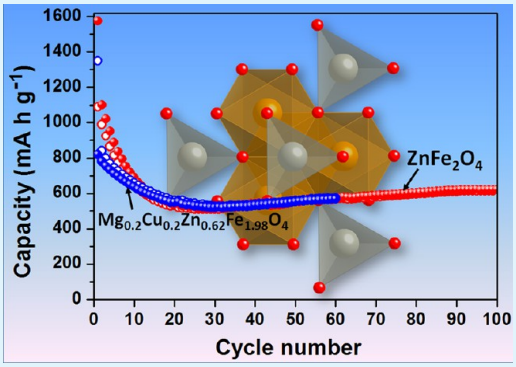

KEYWORDS: *sol–gel method, $ZnFe_2O_4$, Li-ion batteries, anode materials, electrochemical properties*

INTRODUCTION

Lithium ion batteries (LIBs) are widely used in portable electronic devices such as mobile phones, digital cameras, and laptops due to lightweight, compactness, flexibility in design, and environmental friendliness. LIBs have been looked at attentively as the prospective candidate for high-power applications such as hybrid electric vehicles, plug-in electric vehicles, and off-peak energy storage in electric grids.[1] However, for large-scale utilization of high-energy LIBs, various improvements are needed, including identification and development of cheaper and nontoxic electrode materials with enhanced energy density and safer operation at high current rates. Graphite is the commonly used anode material in commercial LIBs owing to its abundance, low cost, longer cycle life, and environmental friendliness. However, it has low specific capacity of 372 mAh g^{-1}. In addition, it also poses safety concerns as Li metal deposition on the graphite anode during charging at high current rates leads to dendrite formation, which can penetrate the microporous separator, resulting in the short-circuiting of LIBs. This led to the quest for alternate safer anode materials that also possess better theoretical capacity compared to that of graphite. Various binary and ternary metal oxides, especially in the form of nanoparticles, have been investigated in the past decade for LIB anodes owing to various advantages such as very high capacity, good volumetric energy density, easy availability, good cyclability, and environmental benignity.[2−4] Among them, notable are TiO_2,[5,6] SnO_2,[7−9] and Fe_2O_3,[10−12] which operate via three distinct mechanisms. TiO_2 with a 2D layer-structure exhibits Li cycling via Li intercalation–deintercalation reaction upon charging and discharging. Oxides like SnO_2,[13] $(M_{1/2}Sb_{1/2}Sn)O_4$ (M = V, Fe, and In)[14,15] undergo lithium storage through alloying and dealloying mechanisms, while many transition metal oxides like Fe_2O_3 have been demonstrated to undergo reversible lithium storage via conversion (redox) reactions.[4]

Recently, various iron-based oxides, MFe_2O_4 (M = Ca, Mg, Ni, Co, Cu, and Zn) have been investigated as anode

Received: April 30, 2014
Accepted: June 9, 2014
Published: June 9, 2014

materials.[16−24] Zinc ferrite, $ZnFe_2O_4$, has a normal spinel structure and can deliver high capacity of ∼1000 mAh g^{-1}. Zn has been found to be a good matrix element, and it can contribute a greater capacity than other ferrite materials due to the alloying−dealloying reaction forming LiZn alloy.[24−26] Electrochemical stability of the anode materials that undergo lithium storage via conversion reaction depends on the material's initial crystal structure, which in turn determines the local environment of the cations that participate in the lithium cycling.[27] Teh et al. investigated the doping of Mn in electrospun $ZnFe_2O_4$ nanofibers; the discharge voltage was slightly lowered and better cyclability was achieved by doping Mn in the spinel anodes.[28] Mixed Zn, Ni ferrites prepared by Cherian et al. showed poor lithium cycling with an increase in the amount of Ni in the sample compared to that of pure Zn-ferrite.[29] Hence, it is of great interest to study the influence of doping atoms such as Mg and Cu on the lithium storage properties of $ZnFe_2O_4$, as these doped compounds also exhibit interesting optical and magnetic properties.[30−32]

In this study, the lithium storage in $Mg_xCu_{0.2}Zn_{0.82-x}Fe_{1.98}O_4$ with varying Mg and Zn content has been investigated. Sol−gel method has been employed to synthesize $ZnFe_2O_4$ and its Mg and Cu codoped samples with compositions of $Mg_xCu_{0.2}Zn_{0.82-x}Fe_{1.98}O_4$ (where x = 0.20, 0.25, 0.30, 0.35, and 0.40). The compounds calcined at 600 °C show large capacity fading, while the samples reheated at 800 °C show better cycling properties.

EXPERIMENTAL SECTION

Synthesis. Nanocrystalline ferrite powders of composition $ZnFe_2O_4$ and $Mg_xCu_{0.2}Zn_{0.82-x}Fe_{1.98}O_4$ (where x = 0.20, 0.25, 0.30, 0.35, and 0.40) were prepared by sol−gel assisted combustion method. In a typical synthesis, stoichiometric amounts of analytical grade $Mg(NO_3)_2{\cdot}4H_2O$, $Cu(NO_3)_2{\cdot}3H_2O$, $Zn(NO_3)_2{\cdot}6H_2O$, and $Fe(NO_3)_3{\cdot}9H_2O$ were dissolved together in distilled water and stirred to obtain a homogeneous solution. An aqueous solution of citric acid, which acts both as fuel and ligand, was then added to the solution containing metal ions such that the molar ratio of citric acid to total metal ions was 1:1. Ammonium hydroxide was added slowly to adjust pH of the solution to 7. The resultant solution was heated at 80 °C, under constant stirring, to transform the solution into a xerogel. On drying, the gel underwent a self-propagating combustion and formed a fluffy powder. The as-burnt powder was calcined in air at 600 °C for 2 h at a heating rate of 10 °C min^{-1} to obtain the single-phase ferrite nanoparticles. The samples were also reheated at 800 °C for 2 h for electrochemical studies.

Structure and Morphological Characterization. The synthesized compounds were characterized by powder X-ray diffraction (PXRD) using a Bruker D5005 diffractometer employing graphite monochromatised Cu Kα radiation (λ = 1.54056 Å). Rietveld refinement of PXRD patterns was performed using TOPAS software (version 2.1). IR spectra of the samples were recorded in the range of 4000−400 cm^{-1} using KBr pellets on Bio-Rad FTS165 FTIR spectrophotometer. Raman spectra of the samples were recorded using the Renishaw Raman system 2000. Brunauer−Emmett−Teller (BET) surface area studies of the powder samples were determined from N_2 adsorption−desorption isotherms at 77 K using TriStar 3000 software (Micromeritics, Norcross, GA). The samples were preheated for 2 h at 180 °C under nitrogen flow to remove adsorbed moisture prior to BET analysis. Morphology of the samples was examined by scanning electron microscopy (SEM) and transmission electron microscopy (TEM). SEM micrographs of the platinum-coated samples were recorded using a JEOL JSM-6700F field emission scanning electron microscope (FESEM) operated at 5 kV and 10 mA. JEOL JEM 2010 (operated at 200 kV) was used to record the TEM images to determine the surface morphology and the particle sizes.

Electrochemical Characterization. Electrochemical properties of the samples were investigated using coin cells (type 2016) with Li metal (Kyokuto Metal Co., Japan) as counter electrode, glass microfiber filter (GF/F, Whatman Int. Ltd., Maidstone, England) as the separator, and 1 M $LiPF_6$ in ethylene carbonate (EC) and diethyl carbonate (DEC) (1:1 v/v, Merck) as the electrolyte. First, a slurry was prepared by mixing the sample (70 wt %) with super P carbon black (15 wt %) and 15 wt % of PVDF binder (Kynar 2801) in *N*-methylpyrrolidinone (NMP) solvent. The slurry was then coated onto an etched copper foil, dried at 80 °C, and cut into circular discs 16 mm in diameter. Coin cells were assembled in an Ar-filled glovebox (MBraun, Germany) with oxygen and water concentration maintained below 1 ppm, by crimp sealing the thus fabricated anode with lithium metal as counter electrode. The cells were aged for 8 h before they were subjected to electrochemical testing. Cyclic voltammetry and galvanostatic discharge−charge cycling studies of the cells were carried out at room temperature using computer-controlled MacPile II (Bio-Logic, France) and Bitrode multiple battery tester (model SCN, Bitrode, Green Park, MO), respectively. Impedance spectroscopy measurements were carried out in the frequency range of 180 kHz to 0.001 Hz using a Solartron 1260A impedance analyzer.

RESULTS AND DISCUSSION

Structure and Morphology. PXRD patterns (Figure 1) of $ZnFe_2O_4$ and $Mg_xCu_{0.2}Zn_{0.82-x}Fe_{1.98}O_4$ (where x = 0.20, 0.25, 0.30, 0.35, and 0.40) reveal the formation of all the compositions in pure phase without any impurities and can be indexed as normal spinel structure (space group *Fd*3*m*). As these ferrites were synthesized by sol−gel assisted combustion route, the ratio of different elements should be the same as the starting materials. To verify the composition of all the phases, inductively coupled plasma (ICP) analyses were carried out. The results reveal that the atomic ratio of the different metals in all the phases are close to the expected values, as shown in Table S1 (Supporting Information). The divalent Zn^{2+} (r_i = 88 pm), Cu^{2+} (r_i = 87 pm), and Mg^{2+} (r_i = 86 pm) ions tend to occupy the tetrahedral sites because of larger size compared to smaller Fe^{3+} ions (r_i = 69 pm), which occupy the octahedral sites. The lattice parameter of the compounds were obtained from Rietveld refinement (Figure 2) using TOPAS software (Table 1). The lattice parameter, a = 8.4483(3) Å, calculated for $ZnFe_2O_4$ is close to the reported values (JCPDS 82-1049). On codoping Mg^{2+} and Cu^{2+} for Zn^{2+}, the lattice parameter

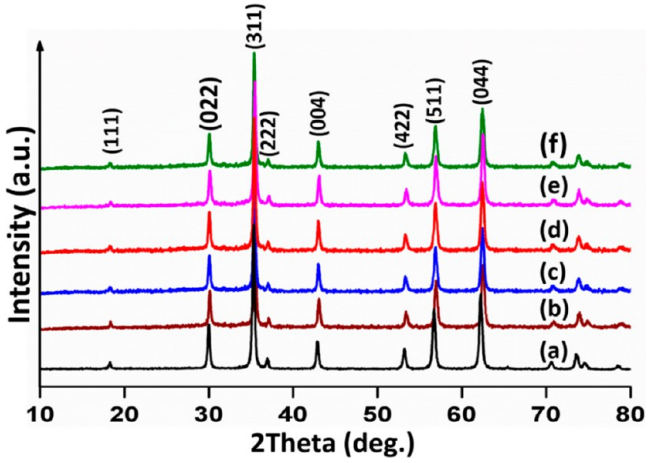

Figure 1. Powder X-ray diffraction (PXRD) patterns of (a) $ZnFe_2O_4$, (b) $Mg_{0.2}Cu_{0.2}Zn_{0.62}Fe_{1.98}O_4$, (c) $Mg_{0.25}Cu_{0.2}Zn_{0.57}Fe_{1.98}O_4$, (d) $Mg_{0.3}Cu_{0.2}Zn_{0.52}Fe_{1.98}O_4$, (e) $Mg_{0.35}Cu_{0.2}Zn_{0.47}Fe_{1.98}O_4$, and (f) $Mg_{0.4}Cu_{0.2}Zn_{0.42}Fe_{1.98}O_4$.

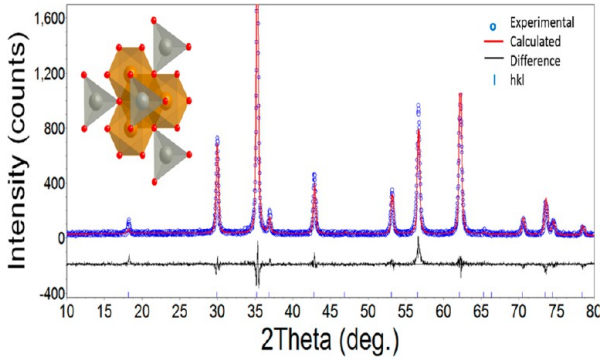

Figure 2. Rietveld refinement of $ZnFe_2O_4$. Blue circles (○) show the experimental values. Red and black lines indicate the calculated pattern and the difference between observed and calculated patterns, respectively. (Inset) Crystallographic representation of $ZnFe_2O_4$ structure.

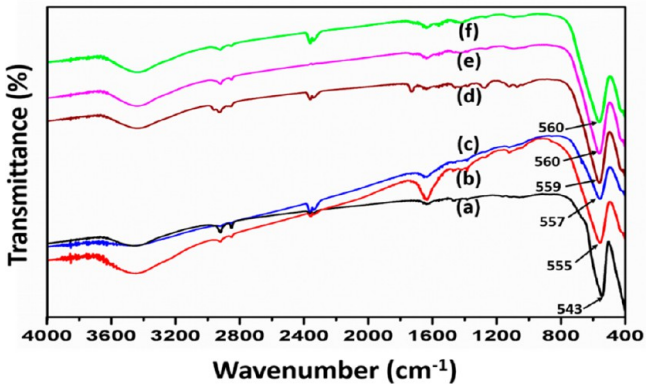

Figure 3. FTIR spectra of (a) $ZnFe_2O_4$, (b) $Mg_{0.2}Cu_{0.2}Zn_{0.62}Fe_{1.98}O_4$, (c) $Mg_{0.25}Cu_{0.2}Zn_{0.57}Fe_{1.98}O_4$, (d) $Mg_{0.3}Cu_{0.2}Zn_{0.52}Fe_{1.98}O_4$, (e) $Mg_{0.35}Cu_{0.2}Zn_{0.47}Fe_{1.98}O_4$, and (f) $Mg_{0.4}Cu_{0.2}Zn_{0.42}Fe_{1.98}O_4$ in the range of 4000−400 cm^{-1}.

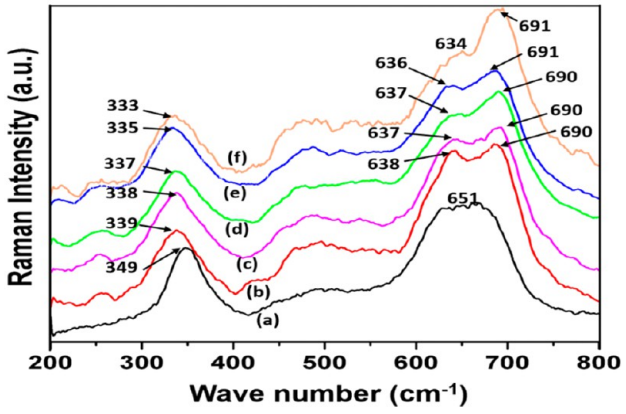

Figure 4. Raman spectra of (a) $ZnFe_2O_4$, (b) $Mg_{0.2}Cu_{0.2}Zn_{0.62}Fe_{1.98}O_4$, (c) $Mg_{0.25}Cu_{0.2}Zn_{0.57}Fe_{1.98}O_4$, (d) $Mg_{0.3}Cu_{0.2}Zn_{0.52}Fe_{1.98}O_4$, (e) $Mg_{0.35}Cu_{0.2}Zn_{0.47}Fe_{1.98}O_4$, and (f) $Mg_{0.4}Cu_{0.2}Zn_{0.42}Fe_{1.98}O_4$.

decreases slightly compared to pure $ZnFe_2O_4$ because of the slightly smaller size of Mg^{2+} and Cu^{2+} ions. Variation of the lattice parameter (a) on varying the amount of Mg^{2+} in the different compositions is given in Table 1. The lattice parameter shows a clear decrease and a linear behavior with increase of Mg^{2+} ion doping. The XRD pattern of $ZnFe_2O_4$ reheated at 800 °C (Figure S1, Supporting Information) suggests that the crystal structure remains the same while the size of the particles increases, as evident from the decrease in peak width.

FTIR spectroscopy is an important technique to identify the stretching and bending vibrations of different materials. IR spectra of the ferrite nanoparticles $ZnFe_2O_4$ and $Mg_xCu_{0.2}Zn_{0.82-x}Fe_{1.98}O_4$ (where x = 0.20, 0.25, 0.30, 0.35, and 0.40) were recorded in the range of 4000−400 cm^{-1}, as shown in Figure 3. In general, stretching vibration due to metal cations present at the tetrahedral site shows a band around 600 cm^{-1}, while the cation present at the octahedral site shows a band around 400 cm^{-1}, which varies slightly depending on the strength of metal−oxygen bond.[33] $ZnFe_2O_4$ nanoparticles show a broad band at 543 cm^{-1} characteristic of Zn−O vibration as Zn^{2+} is present at the tetrahedral site. On doping $ZnFe_2O_4$, Mg^{2+} and Cu^{2+} replace Zn^{2+} from the tetrahedral site, and the band shifts to higher wavenumbers, as seen in Figure 3. For $Mg_{0.2}Cu_{0.2}Zn_{0.62}Fe_{1.98}O_4$, the peak shifts to 555 cm^{-1} compared to 543 cm^{-1} of the undoped $ZnFe_2O_4$, which can be attributed to stronger Mg−O bond. With further increase in the Mg^{2+} content, vibrational energy increases slightly and becomes 560 cm^{-1} when the Mg content becomes 0.4 (Figure 3f).

Raman spectra of all the compositions recorded at room temperature are shown in Figure 4. $ZnFe_2O_4$ exhibits normal spinel structure for which five active Raman modes (A_{1g} + E_g + $3T_{2g}$) are possible. Usually, the motion of oxygen at tetrahedral sites in the spinel compounds give bands above 600 cm^{-1} that are of the A_{1g} type. The band at ∼650 cm^{-1} for $ZnFe_2O_4$ corresponds to motion of oxygen in the ZnO_4 tetrahedra. Similar bands were observed for $ZnFe_2O_4$ obtained by Yao et al.[34] Upon doping the band splits into two at ∼638 and 690 cm^{-1} due to the change in the environment of the tetrahedra.

SEM micrographs of the as-synthesized nanoparticles are shown in Figure 5. The SEM images reveal the formation of $ZnFe_2O_4$ and the doped compounds in the form of nanoparticles. The average crystallite sizes of the compounds are calculated to be 56−75 nm using Scherrer's equation and are given in Table 1. The individual nanoparticles are closely packed to form micrometer sized particles. The surface morphology of the different compositions appear to be slightly different from each other. TEM images of $ZnFe_2O_4$ and $Mg_{0.2}Cu_{0.2}Zn_{0.62}Fe_{1.98}O_4$ are shown in Figure 6, panels a and b,

Table 1. Lattice Parameter, Refinement Details, and Surface Area of Various Compositions

compound	lattice parameter a (Å)	R_{wp} (%)	R_B (%)	GOF	BET surface area (±0.05 m^2 g^{-1})	average crystallite size (nm)
$ZnFe_2O_4$	8.4483(3)	14.95	5.94	1.28	10.5	61
$Mg_{0.2}Cu_{0.2}Zn_{0.62}Fe_{1.98}O_4$	8.4249(4)	14.26	3.64	1.24	11.5	71
$Mg_{0.25}Cu_{0.2}Zn_{0.57}Fe_{1.98}O_4$	8.4247(5)	14.43	3.77	1.21	11.8	56
$Mg_{0.3}Cu_{0.2}Zn_{0.52}Fe_{1.98}O_4$	8.4225(5)	14.34	4.08	1.24	12.8	61
$Mg_{0.35}Cu_{0.2}Zn_{0.47}Fe_{1.98}O_4$	8.4195(5)	14.62	4.05	1.26	11.1	75
$Mg_{0.4}Cu_{0.2}Zn_{0.42}Fe_{1.98}O_4$	8.4192(5)	14.78	4.36	1.27	11.5	65

dx.doi.org/10.1021/am502605s | ACS Appl. Mater. Interfaces 2014, 6, 10744−10753

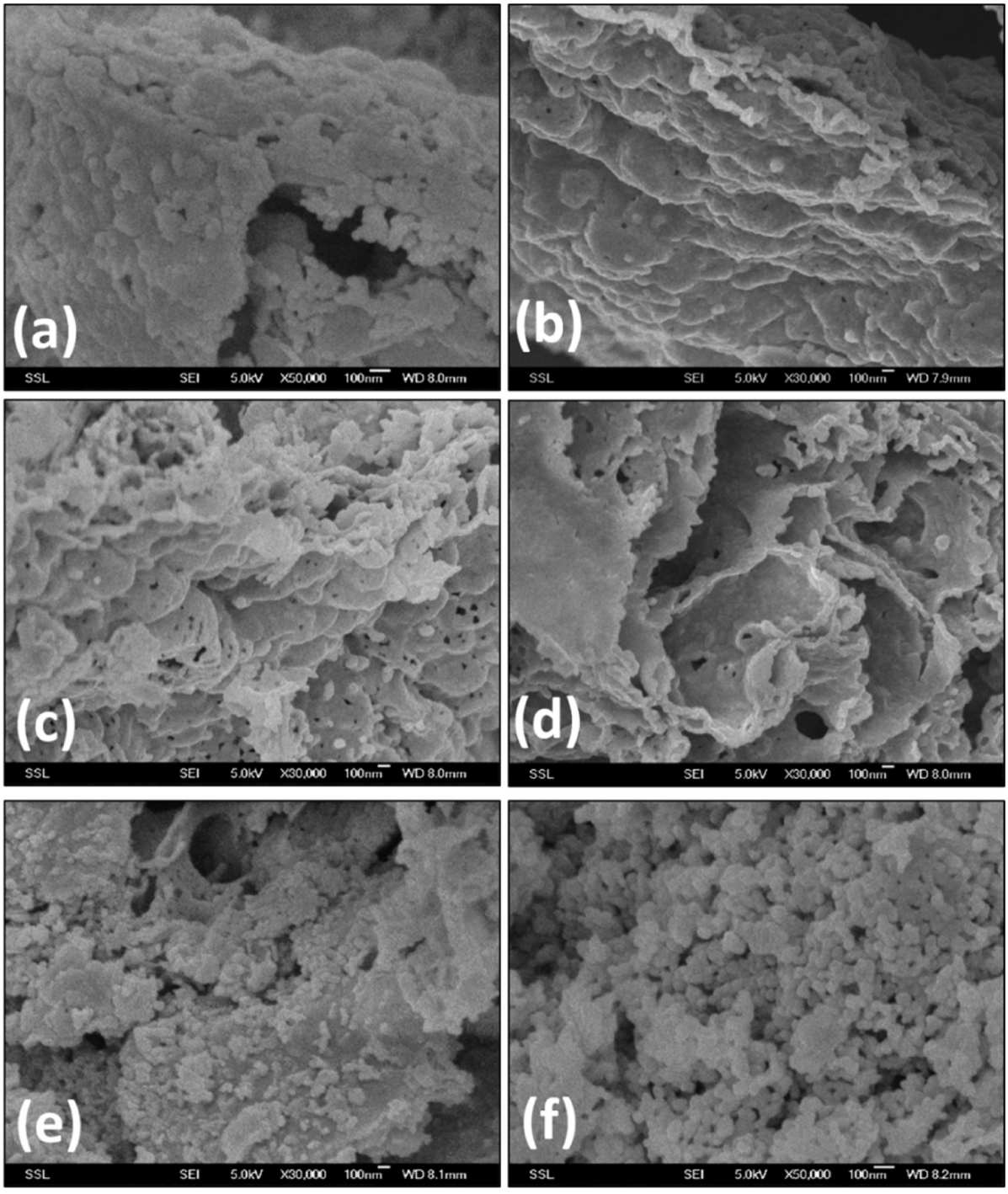

Figure 5. SEM images of (a) $ZnFe_2O_4$, (b) $Mg_{0.2}Cu_{0.2}Zn_{0.62}Fe_{1.98}O_4$, (c) $Mg_{0.25}Cu_{0.2}Zn_{0.57}Fe_{1.98}O_4$, (d) $Mg_{0.3}Cu_{0.2}Zn_{0.52}Fe_{1.98}O_4$, (e) $Mg_{0.35}Cu_{0.2}Zn_{0.47}Fe_{1.98}O_4$, and (f) $Mg_{0.4}Cu_{0.2}Zn_{0.42}Fe_{1.98}O_4$ calcined at 600 °C using sol−gel method.

respectively. The particle size was found to be ∼50 nm, which is in agreement with the crystallite size calculated from Scherrer's equation. The HR-TEM image of $ZnFe_2O_4$ (Figure 6c) shows lattice fringes with interplanar spacing (d) of 4.79 Å, corresponding to (111) planes, and d spacing of 2.09 Å for $Mg_{0.2}Cu_{0.2}Zn_{0.62}Fe_{1.98}O_4$ (Figure 6d), corresponding to (400) planes. The BET nitrogen adsorption−desorption analysis at 77 K was used to determine the specific surface area of the different compositions. The compounds exhibit type IV nitrogen isotherm (Figure S2, Supporting Information) that proceeds via multilayer adsorption followed by capillary condensation. The surface area of the different compositions were calculated to be in the range ∼11−12 $m^2\ g^{-1}$, which suggests good porosity of the sol−gel prepared samples. The BET surface area of the different compositions are given in Table 1, and doping does not have much influence on the surface area because the samples are prepared at identical temperatures.

Electrochemical Studies. *Galvanostatic Cycling.* Galvanostatic charge−discharge cycling studies were carried out to investigate the Li storage and cyclability of all the compositions in the voltage window of 0.005−3.0 V vs Li/Li^+ at a current

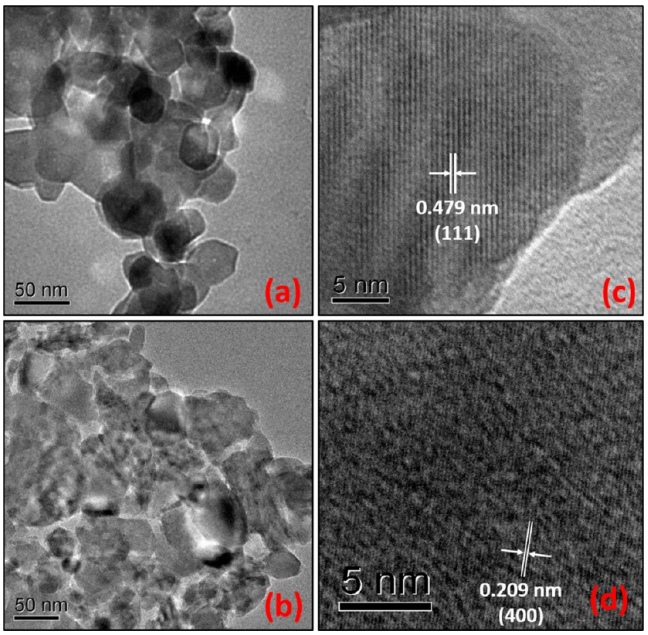

Figure 6. TEM images of (a) $ZnFe_2O_4$, (b) $Mg_{0.2}Cu_{0.2}Zn_{0.62}Fe_{1.98}O_4$, (c) HR-TEM showing lattice fringes of $ZnFe_2O_4$, and (d) HR-TEM image of $Mg_{0.2}Cu_{0.2}Zn_{0.62}Fe_{1.98}O_4$.

density of 100 mA g^{-1}. Voltage versus capacity profiles of the first cycle of the as-prepared samples and the reheated (800 °C) samples are shown in Figure 7, panels a and b, respectively. The first discharge curve of $ZnFe_2O_4$ (Figure 7a) starts from the open circuit voltage (~2.5 V) and shows a steep decrease with two small plateaus at ~1.5 and 0.9 V that are due to Li intercalation into $ZnFe_2O_4$ to form $Li_xZnFe_2O_4$ ($x \approx 2$) according to eq 1.[4,24] Similar intercalation reaction were also observed for the doped compounds at 1.5−1.3 and 1.0−0.9 V. Further reaction of Li with the intercalated phase (as indicated by the large plateau at ~0.8 V) leads to crystal structure destruction of $ZnFe_2O_4$ accompanied by reduction of metal ions to metal nanoparticles (Fe, Zn) embedded in an amorphous matrix of Li_2O according to eq 2. In the case of doped compounds, lithiation occurs at ~0.7−0.8 V and forms Zn, Fe, Cu, and MgO nanoparticles embedded in Li_2O matrix. Mg is an electrochemically inactive metal that does not involve in the lithium storage, while Cu is an electroactive metal and takes part in lithium storage similar to Zn. The Zn nanoparticles also undergo alloying reaction with Li beyond the plateau region to form Li−Zn alloy as per eq 3.[4,24]

During the first charge cycle (Li extraction), the dealloying reaction occurs first according to eq 3, followed by the reaction of metal nanoparticles with Li_2O to form a mixture of ZnO and Fe_2O_3 instead of the initial spinel ferrite phase as per eq 4. In the doped samples, Cu, Zn, and Fe nanoparticles react with Li_2O and form a mixture of the corresponding oxides. The second discharge curve shows a different profile compared to the first cycle, suggesting the mechanism is different and the reversible lithium storage is due to the reversible conversion of metal oxides to metal nanoparticles embedded in Li_2O, according to eq 4, which is repeated in the subsequent cycles.

$$ZnFe_2O_4 + xLi^+ + xe^- \rightarrow Li_xZnFe_2O_4 \quad (1)$$

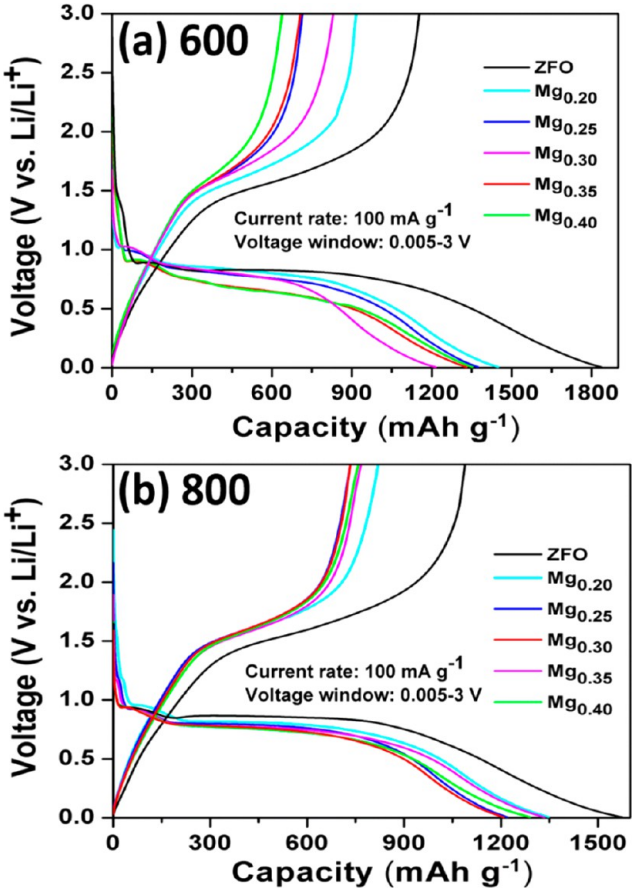

Figure 7. First galvanostatic charge−discharge cycle of $ZnFe_2O_4$ and $Mg_xCu_{0.2}Zn_{0.82-x}Fe_{1.98}O_4$ (where x = 0.20, 0.25, 0.30, 0.35, and 0.40) (a) calcined at 600 °C and (b) reheated at 800 °C.

$$Li_xZnFe_2O_4 + (8 - x)Li^+ + (8 - x)e^- \rightarrow Zn + 2Fe + 4Li_2O \quad (2)$$

$$Zn + Li^+ + e^- \leftrightarrow LiZn \quad (3)$$

$$Zn + 2Fe + 4Li_2O \leftrightarrow ZnO + Fe_2O_3 + 8Li^+ + 8e^- \quad (4)$$

One mole of $ZnFe_2O_4$ reacts with 9 mol of Li as per eqs 3 and 4, resulting in a total reversible capacity of 1000 mAh g^{-1}. The theoretical capacity of doped compounds $Mg_xCu_{0.2}Zn_{0.82-x}Fe_{1.98}O_4$ decreases slightly compared to that of $ZnFe_2O_4$. This is due to incomplete reduction of $Mg_xCu_{0.2}Zn_{0.82-x}Fe_{1.98}O_4$ forming MgO along with Zn, Cu, and Fe nanoparticles during the first discharge cycle. For x = 0.2, the theoretical capacity is 945, which further decreases to 910 mAh g^{-1} for x = 0.4. The first charge−discharge profiles of the different compositions calcined at 600 °C are shown in Figure 7a. The initial discharge capacity of $ZnFe_2O_4$ was found to be 1836 mAh g^{-1}, while the doped samples show capacities of 1210−1449 mAh g^{-1}. The first discharge capacity of $ZnFe_2O_4$ was 1153 mAh g^{-1} and the doped samples show capacities in the range of 629−920 mAh g^{-1}. Detailed cycling results for all the compositions are given in Figures S3 and S4 (Supporting Information). The additional capacity, more than the theoretical capacity, can be attributed to solid electrolyte interface (SEI) formation by consumption of Li during discharge. At the end of 60 cycles, the capacity of $ZnFe_2O_4$ decreases to 332 mAh g^{-1}. The details of the charge and

Table 2. Charge and Discharge Capacities for the 1st, 2nd, and 60th Cycles of the As-Synthesized (600 °C) Samples

	discharge capacity (mAh g^{-1})			charge capacity (mAh g^{-1})		
compound	1st cycle	2nd cycle	60th cycle	1st cycle	2nd cycle	60th cycle
$ZnFe_2O_4$	1836	1176	332 (60th) 343 (100th)	1153	989	328 (60th) 340 (100th)
$Mg_{0.2}Cu_{0.2}Zn_{0.62}Fe_{1.98}O_4$	1450	931	547	929	836	534
$Mg_{0.25}Cu_{0.2}Zn_{0.57}Fe_{1.98}O_4$	1374	704	335	714	567	340
$Mg_{0.3}Cu_{0.2}Zn_{0.52}Fe_{1.98}O_4$	1290	769	264 (50th)	642	493	255 (50th)
$Mg_{0.35}Cu_{0.2}Zn_{0.47}Fe_{1.98}O_4$	1330	697	223	707	512	218
$Mg_{0.4}Cu_{0.2}Zn_{0.42}Fe_{1.98}O_4$	1353	630	203	639	512	201

discharge capacities of the individual samples for the 1st and 60th cycles are tabulated in Table 2. Capacity versus cycle number plots of all compositions calcined at 600 °C are shown in Figure 8a,b. The composite, $Mg_{0.2}Cu_{0.2}Zn_{0.62}Fe_{1.98}O_4$ shows better cyclability than the other compositions, as seen from Figure 8b.

The samples were also reheated to 800 °C for 2 h in air and the electrochemical studies were repeated. Their first discharge−charge profiles are shown in Figure 7b. The charge and discharge capacities of all the doped compositions are found to be in a similar range. The initial discharge capacities are in the range of 1208−1348 (±10) mAh g^{-1} for the doped samples and 1575 mAh g^{-1} for pure $ZnFe_2O_4$. The details of the charge and discharge capacities for the 1st and 60th cycles for the reheated samples are given in Table 3. At the end of 60 cycles, the capacity of $ZnFe_2O_4$ decreases to 575 mAh g^{-1}, while the doped compounds show capacities of 576−543 mAh g^{-1}. As shown in Figure 7, the reheated samples show a better capacity retention than the as-synthesized samples. $ZnFe_2O_4$ reheated at 800 °C shows a reversible capacity of 620 mAh g^{-1} for the 100th cycle. In comparison, the as-synthesized $ZnFe_2O_4$ shows a reversible capacity of only 343 mAh g^{-1} for the 100th cycle. The improved capacity retention for the samples reheated at 800 °C can be attributed to proper ordering of crystal structure and decrease in the electrode resistance. Tirado et al.[19] noted a similar improvement of capacity values with increased synthesis temperature for Fe-based oxides by group. $ZnFe_2O_4$ prepared by urea combustion method showed a similar capacity of 615 mAh g^{-1} at a current density of 60 mA g^{-1}.[24] Carbon-coated and graphene composites of $ZnFe_2O_4$ have been found to exhibit high capacity due to better conductivity.[23,34−39]

The capacity was observed as fading during the initial 10−15 cycles and then stabilized or increased slightly. A similar trend was observed in $NiFe_2O_4$ by Tirado et al., where the capacity decay occurred during first 20 cycles irrespective of the preparation conditions, and then the capacity of the material stabilized.[19] This capacity loss can be due to the "formation" or "conditioning" of the electrode, referred to as electrochemical grinding effect during the initial cycles, which disintegrates the Li_2O matrix and Zn−Fe nanoparticles. The slight increase in the capacity during later cycles has been observed in various other anode materials like Fe_3O_4 and Zn_2MnO_4.[40,41] This can be attributed to the reversible growth of a polymeric gel-like film occurring as a result of electrolyte decomposition. Of the doped compounds, $Mg_{0.2}Cu_{0.2}Zn_{0.62}Fe_{1.98}O_4$ shows the best performance (Figure 8b,c). Reversible capacities of 547 and 576 mAh g^{-1}, respectively, were obtained for the as-synthesized and reheated $Mg_{0.2}Cu_{0.2}Zn_{0.62}Fe_{1.98}O_4$ after 60 cycles. The galvanostatic cycling of the reheated samples was also carried out at higher current densities of 500 and 1000 mA g^{-1}.

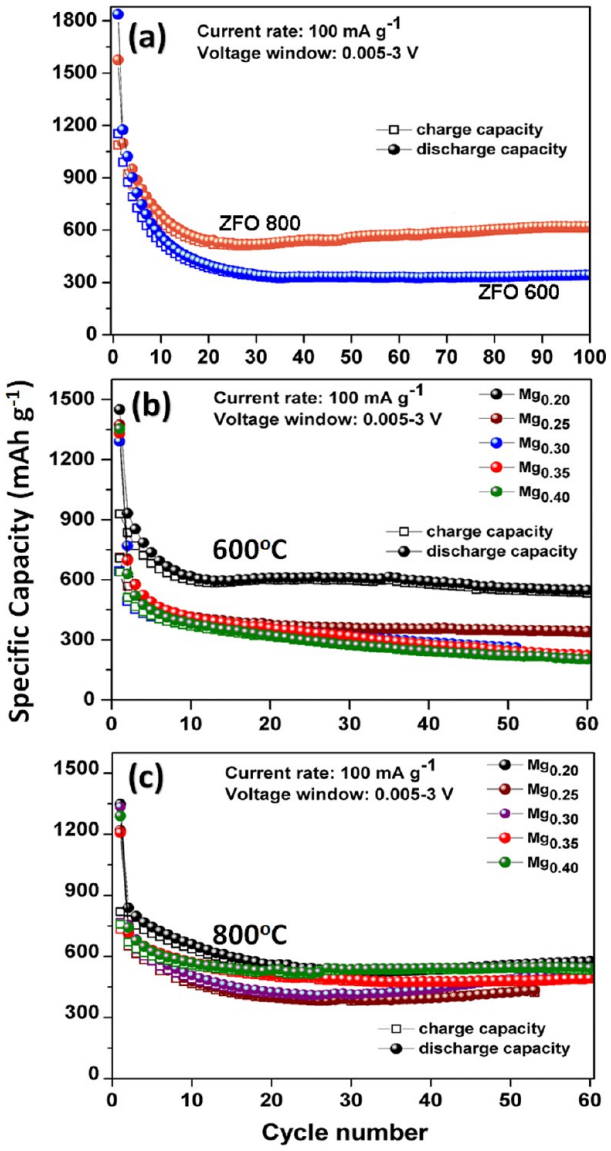

Figure 8. Comparison of cycling stability of (a) $ZnFe_2O_4$ calcined at 600 and 800 °C, (b) $Mg_xCu_{0.2}Zn_{0.82-x}Fe_{1.98}O_4$ (where x = 0.20, 0.25, 0.30, 0.35, and 0.40) calcined at 600 °C, and (c) $Mg_xCu_{0.2}Zn_{0.82-x}Fe_{1.98}O_4$ reheated at 800 °C.

$Mg_{0.2}Cu_{0.2}Zn_{0.62}Fe_{1.98}O_4$ exhibits a capacity of 410 and 328 mAh g^{-1} at 500 and 1000 mA g^{-1}, respectively, which is slightly higher than that of $ZnFe_2O_4$. The capacity versus cycle number plots at higher current are shown in Figure S5 (Supporting Information).

Table 3. Charge and Discharge Capacities for the 1st, 2nd, and 60th Cycles of the Compounds Reheated at 800 °C

	discharge capacity (mAh g^{-1})			charge capacity (mAh g^{-1})		
compound	1st cycle	2nd cycle	60th cycle	1st cycle	2nd cycle	60th cycle
$ZnFe_2O_4$	1575	1100	575 (60th) 620 (100th)	1089	989	567 (60th) 612 (100th)
$Mg_{0.2}Cu_{0.2}Zn_{0.62}Fe_{1.98}O_4$	1348	840	576	820	781	568
$Mg_{0.25}Cu_{0.2}Zn_{0.57}Fe_{1.98}O_4$	1220	719	433 (50th)	734	652	423 (50th)
$Mg_{0.3}Cu_{0.2}Zn_{0.52}Fe_{1.98}O_4$	1334	757	535	767	678	533
$Mg_{0.35}Cu_{0.2}Zn_{0.47}Fe_{1.98}O_4$	1208	714	492	734	671	488
$Mg_{0.4}Cu_{0.2}Zn_{0.42}Fe_{1.98}O_4$	1290	742	543	759	671	533

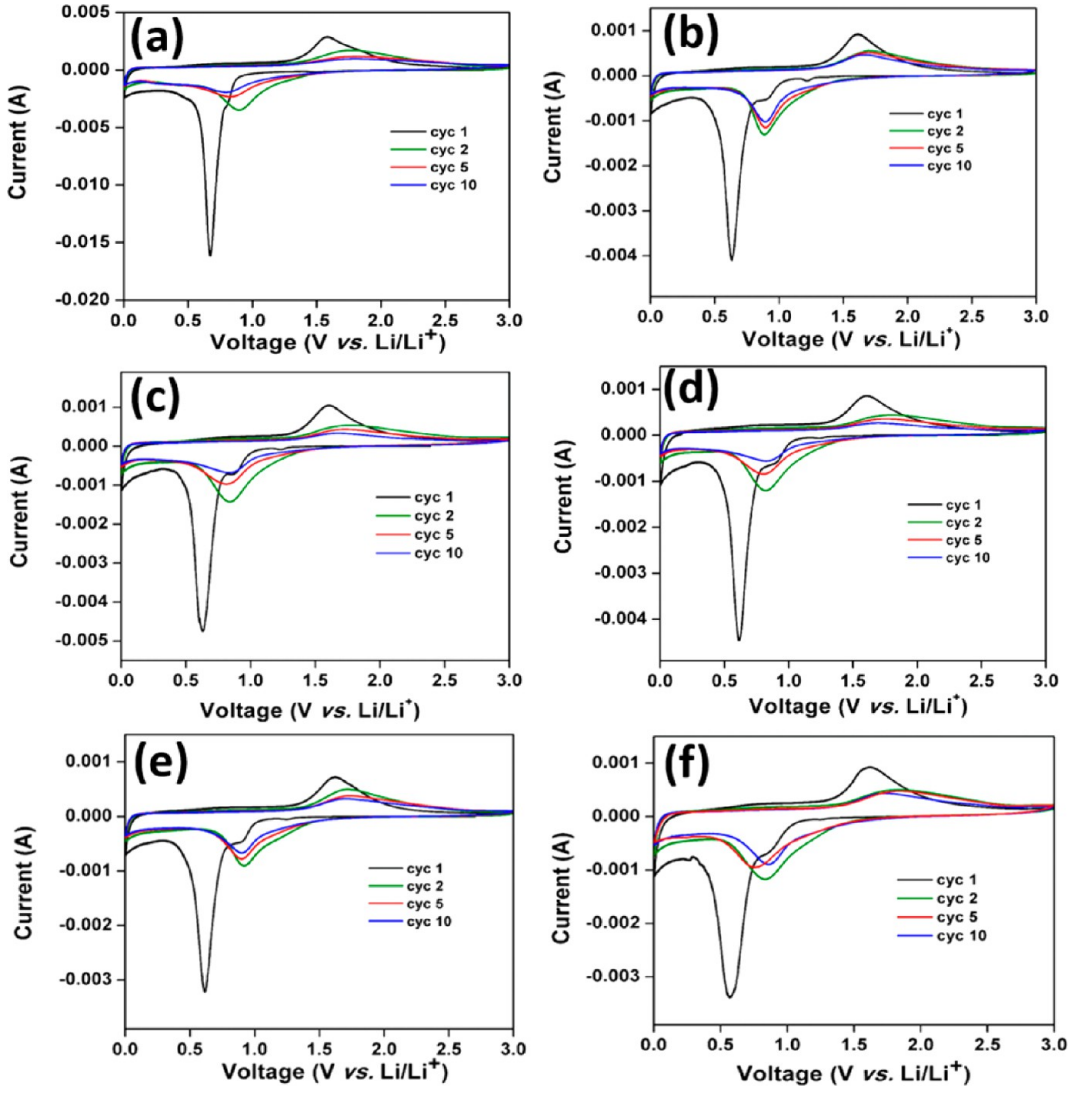

Figure 9. Cyclic voltammograms (CV) of (a) $ZnFe_2O_4$, (b) $Mg_{0.20}Cu_{0.20}Zn_{0.62}Fe_{1.98}O_4$, (c) $Mg_{0.25}Cu_{0.20}Zn_{0.57}Fe_{1.98}O_4$, (d) $Mg_{0.30}Cu_{0.20}Zn_{0.52}Fe_{1.98}O_4$, (e) $Mg_{0.35}Cu_{0.20}Zn_{0.47}Fe_{1.98}O_4$, and (f) $Mg_{0.40}Cu_{0.20}Zn_{0.42}Fe_{1.98}O_4$ reheated at 800 °C at a scan rate of 0.058 mV s^{-1} in the potential range, 0.005−3.0 V.

Cyclic Voltammetry. $ZnFe_2O_4$ and the doped composites were also characterized by cyclic voltammetry (CV) in the voltage window of 0.005−3.0 V vs Li/Li^+ at a scan rate of 0.058 mV s^{-1} at room temperature using Li metal as the counter and reference electrode. The cyclic voltammograms of different compositions are shown in Figure 9. For clarity, only selected cycles are shown. For all the compositions, it is clear that the first cathodic scan is distinct from the subsequent cycles, as observed in the galvanostatic cycling. During the first cathodic scan (discharge cycle) of $ZnFe_2O_4$ (Figure 9a), Li-intercalation occurs into the compound (as evidenced by small peaks at 1.5 and 0.8 V) and involves reduction of Fe(III) in $ZnFe_2O_4$ to form the intercalation phase $Li_xZnFe_2O_4$. Further lithiation occurs at ∼0.7 V as indicated by the sharp peak in CV, leading to crystal structure destruction, which involves the reduction of Zn(II) and Fe(II) and formation of Zn and Fe nanoparticles embedded in a matrix of Li_2O, as described earlier in eq 1. During the first charge cycle, anodic peak is observed at 1.6 V

dx.doi.org/10.1021/am502605s | ACS Appl. Mater. Interfaces 2014, 6, 10744−10753

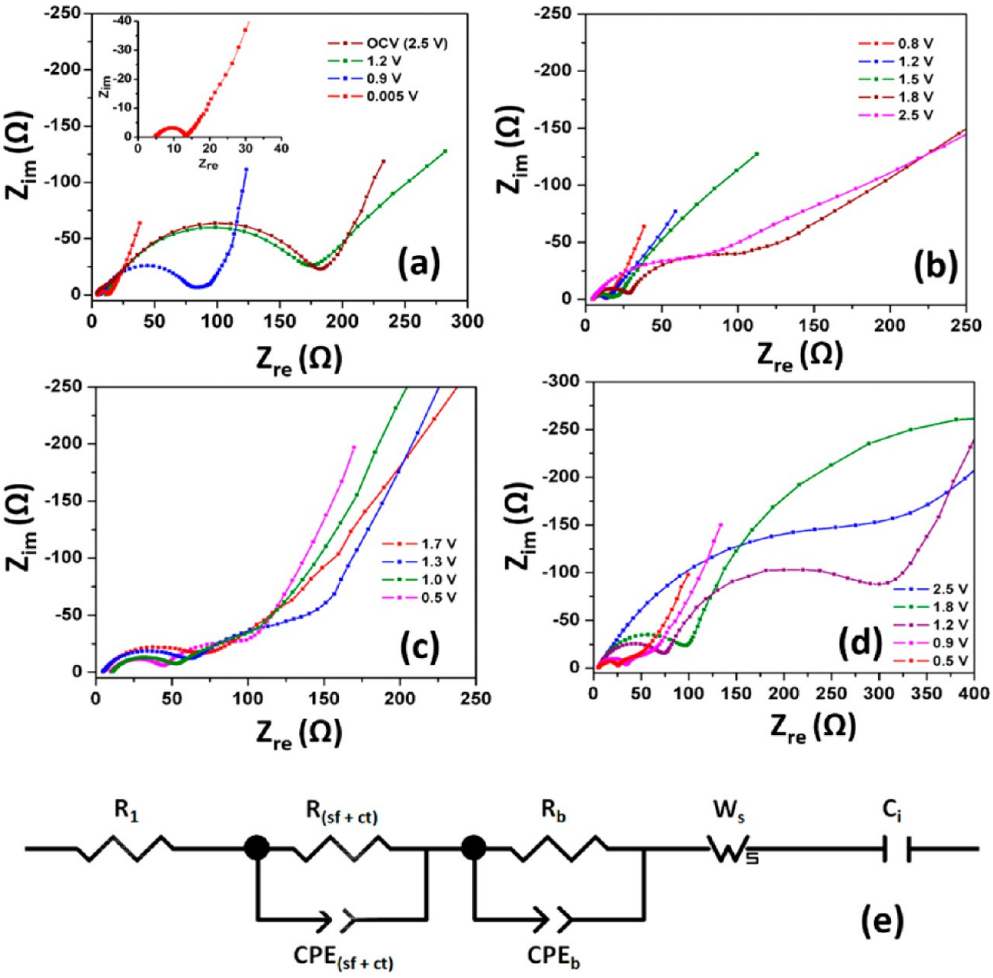

Figure 10. Nyquist plots of $ZnFe_2O_4$ (reheated at 800 °C) at selected voltages during (a) 1st discharge cycle, (b) 1st charge cycle, (c) 10th discharge cycle, and (d) 10th charge cycle. (e) Equivalent circuit for the observed Nyquist plots.

and it is attributed to the oxidation of Fe and Zn to the respective metal oxides. Compared to the first cycle, the cathodic peak in the second and subsequent cycles shift from 0.7 to ∼0.8−0.9 V and became broad for all the compositions. The anodic peak of the second and subsequent cycles also became broad and shifted to ∼1.7−1.8 V, which is consistent with the galvanostatic cycling results. The capacity fading was found to be minimum for $Mg_{0.2}Cu_{0.2}Zn_{0.62}Fe_{1.98}O_4$, which is consistent with the galvanostatic cycling results.

Electrochemical Impedance Spectroscopy (EIS) Studies. Electrochemical impedance spectroscopy is one widely used and powerful analytical technique employed to analyze the electrode kinetics.[42−44] EIS measurements were carried out for as-synthesized and reheated $ZnFe_2O_4$ samples during the 1st and 10th charge and discharge cycles at selected voltages (Figure 10). During each voltage increment (charging) and decrement (discharging), the cell was subjected to a current density of ∼200 mA g^{-1} and was relaxed at the given voltage for 2 h before data collection. The results are plotted as Nyquist plots (Z_{re} vs Z_{im}), where Z_{re} and Z_{im} are the real and imaginary parts of cell impedance, respectively.

The Nyquist plot for the data collected at open circuit voltage (2.5 V) for reheated (800 °C) $ZnFe_2O_4$ showed a single semicircle with an overall impedance of ∼180 Ω in the high- to medium-frequency range, which can be attributed to the surface film and charge transfer resistance ($R_{sf} + R_{ct}$) and the associated capacitances (CPE_{sf} and CPE_{dl}), though a single semicircle was observed. The equivalent circuit for the observed Nyquist plots is shown in Figure 10e. At 0.9 V, where the lithium intercalation into $ZnFe_2O_4$ happens, the impedance decreases to ∼80 Ω. When the cell was discharged to 0.005 V, the impedance became 13 Ω, indicating better conductivity at the fully discharged state due to the presence of metal ions embedded in the Li_2O matrix. During the first charge (delithiation) cycle, the observed impedance until 1.2 V was ∼13 Ω, with a single semicircle similar to the first discharge cycle at lower voltages. With further increase in the voltage, a second semicircle corresponding to the bulk resistance was observed; the bulk resistance increases with increase in voltage, as can be seen in Figure 10b. After few charge−discharge cycles, the impedance was measured again for the 10th cycle (charge and discharge). During the charge and discharge cycles, there are two semicircles. The bigger semicircle at the low-frequency region indicates the dominance of bulk resistance, which arises due to decreasing electronic conductivity of active material, ionic conductivity of electrolyte filled in the pores of the composite electrode.[45] The observed overall impedance was found to be higher than that of the first cycle. The effect of increased impedance can be observed in the galvanostatic cycling results in the form of decreased capacity. The increase in the impedance results in the capacity fading during the initial few cycles, after which the capacity becomes stable. The overall

impedance of the reheated sample was less than that of the as-synthesized samples at 600 °C (Figure S6, Supporting Information), which accounts for the improvement in the lithium cycling for the reheated sample compared to the as-synthesized sample.

CONCLUSIONS

We have successfully synthesized $ZnFe_2O_4$ and (Mg, Cu) codoped composites of formula $Mg_xCu_{0.2}Zn_{0.82-x}Fe_{1.98}O_4$ (where x = 0.20, 0.25, 0.30, 0.35, and 0.40) using sol–gel assisted combustion method. The synthesized materials characterized by XRD, SEM, TEM, and BET surface area studies are found to contain nanoparticles 50–80 nm in size. Galvanostatic cycling of $ZnFe_2O_4$ prepared at 800 °C exhibits first charge capacity of 1089 mAh g^{-1} at 100 mA g^{-1} in the voltage range of 0.005–3.0 V. At the end of the 100th cycle, it exhibits a high and stable reversible capacity of ~612 (±5) mAh g^{-1}. Though the (Mg, Cu) codoped compounds exhibit less theoretical capacity, $Mg_{0.2}Cu_{0.2}Zn_{0.62}Fe_{1.98}O_4$ exhibits good reversible capacity and better capacity retention than $ZnFe_2O_4$ nanoparticles, especially at higher current rates. The reversible capacity of the samples was improved by annealing at a higher temperature of 800 °C. However, there is still capacity fading during the initial few cycles, which can be minimized with the help of carbon coating or by preparing graphene-$Mg_{0.2}Cu_{0.2}Zn_{0.62}Fe_{1.98}O_4$ composites.

ASSOCIATED CONTENT

Supporting Information

Additional information on compound characterization. This material is available free of charge via the Internet at http://pubs.acs.org.

AUTHOR INFORMATION

Corresponding Author

*E-mail: phymvvr@nus.edu.sg, msemvvr@nus.edu.sg, reddymvvr@gmail.com. Tel.: +65-65162607. Fax: +65-67776126.

Notes

The authors declare no competing financial interest.

ACKNOWLEDGMENTS

A.S.H. acknowledges NUS for the research scholarship. H.B. thanks people in the Advanced Battery Lab, Department of Physics, NUS for their guidance and encouragement and acknowledges Malayer University for financial support.

REFERENCES

(1) Goodenough, J. B.; Park, K.-S. The Li-Ion Rechargeable Battery: A Perspective. *J. Am. Chem. Soc.* **2013**, *135*, 1167–1176.
(2) Ji, L.; Lin, Z.; Alcoutlabi, M.; Zhang, X. Recent Developments in Nanostructured Anode Materials for Rechargeable Lithium-Ion Batteries. *Energy Environ. Sci.* **2011**, *4*, 2682–2699.
(3) Wei, W.; Wang, Z.; Liu, Z.; Liu, Y.; He, L.; Chen, D.; Umar, A.; Guo, L.; Li, J. Metal Oxide Hollow Nanostructures: Fabrication and Li Storage Performance. *J. Power Sources* **2013**, *238*, 376–387.
(4) Reddy, M. V.; Subba Rao, G. V.; Chowdari, B. V. R. Metal Oxides and Oxysalts as Anode Materials for Li Ion Batteries. *Chem. Rev.* **2013**, *113*, 5364–5457.
(5) Armstrong, A. R.; Armstrong, G.; Canales, J.; Bruce, P. G. TiO_2-B Nanowires. *Angew. Chem., Int. Ed.* **2004**, *43*, 2286–2288.
(6) Lee, S.; Ha, J.; Choi, J.; Song, T.; Lee, J. W.; Paik, U. 3D Cross-Linked Nanoweb Architecture of Binder-Free TiO_2 Electrodes for Lithium Ion Batteries. *ACS Appl. Mater. Interfaces* **2013**, *5*, 11525–11529.
(7) Su, Y.; Li, S.; Wu, D.; Zhang, F.; Liang, H.; Gao, P.; Cheng, C.; Feng, X. Two-Dimensional Carbon-Coated Graphene/Metal Oxide Hybrids for Enhanced Lithium Storage. *ACS Nano* **2012**, *6*, 8349–8356.
(8) Paek, S.-M.; Yoo, E.; Honma, I. Enhanced Cyclic Performance and Lithium Storage Capacity of SnO_2/Graphene Nanoporous Electrodes with Three-Dimensionally Delaminated Flexible Structure. *Nano Lett.* **2009**, *9*, 72–75.
(9) Idota, Y.; Kubota, T.; Matsufuji, A.; Maekawa, Y.; Miyasaka, T. Tin-Based Amorphous Oxide: A High-Capacity Lithium-Ion-Storage Material. *Science* **1997**, *276*, 1395–1397.
(10) Lee, S.-H.; Sridhar, V.; Jung, J.-H.; Karthikeyan, K.; Lee, Y.-S.; Mukherjee, R.; Koratkar, N.; Oh, I.-K. Graphene-Nanotube-Iron Hierarchical Nanostructure as Lithium Ion Battery Anode. *ACS Nano* **2013**, *7*, 4242–4251.
(11) Reddy, M. V.; Yu, T.; Sow, C.-H.; Shen, Z. X.; Lim, C. T.; Rao, G. V. S.; Chowdari, B. V. R. α-Fe_2O_3 Nanoflakes as an Anode Material for Li-Ion Batteries. *Adv. Funct. Mater.* **2007**, *17*, 2792–2799.
(12) Zhu, X.; Zhu, Y.; Murali, S.; Stoller, M. D.; Ruoff, R. S. Nanostructured Reduced Graphene Oxide/Fe_2O_3 Composite as a High-Performance Anode Material for Lithium Ion Batteries. *ACS Nano* **2011**, *5*, 3333–3338.
(13) Courtney, I. A.; Dahn, J. R. Key Factors Controlling the Reversibility of the Reaction of Lithium with SnO_2 and Sn_2BPO_6 Glass. *J. Electrochem. Soc.* **1997**, *144*, 2943–2948.
(14) Reddy, M. V.; Subba Rao, G. V.; Chowdari, B. V. R. Li-storage and Cycling properties of Sn–Sb-mixed oxides, $(M_{1/2}Sb_{1/2}Sn)O_4$, M = In, Fe. *J. Solid State Electrochem.* **2013**, *17*, 1765–1773.
(15) Reddy, M. V.; Subba Rao, G. V.; Chowdari, B. V. R. Nano-$(V_{1/2}Sb_{1/2}Sn)O_4$: A High Capacity, High Rate Anode Material for Li-Ion Batteries. *J. Mater. Chem.* **2011**, *21*, 10003–10011.
(16) Jung, Y. H.; Kim, D. K.; Hong, S.-T. Synthesis, Structure, and Electrochemical Li-Ion Intercalation of $LiRu_2O_4$ with $CaFe_2O_4$-Type Structure. *J. Power Sources* **2013**, *233*, 285–289.
(17) Sharma, N.; Shaju, K. M.; Subba, R. G. V.; Chowdari, B. V. R. Iron-Tin Oxides with $CaFe_2O_4$ structure as Anodes for Li-Ion Batteries. *J. Power Sources* **2003**, *124*, 204–212.
(18) Gong, C.; Bai, Y.-J.; Qi, Y.-X.; Lun, N.; Feng, J. Preparation of Carbon-Coated $MgFe_2O_4$ with Excellent Cycling and Rate Performance. *Electrochim. Acta* **2013**, *90*, 119–127.
(19) Lavela, P.; Tirado, J. L. $CoFe_2O_4$ and $NiFe_2O_4$ Synthesized by Sol-gel Procedures for their Use as Anode Materials for Li Ion Batteries. *J. Power Sources* **2007**, *172*, 379–387.
(20) Cherian, C. T.; Sundaramurthy, J.; Reddy, M. V.; Suresh, K. P.; Mani, K.; Pliszka, D.; Sow, C. H.; Ramakrishna, S.; Chowdari, B. V. R. Morphologically Robust $NiFe_2O_4$ Nanofibers as High Capacity Li-Ion Battery Anode Material. *ACS Appl. Mater. Interfaces* **2013**, *5*, 9957–9963.
(21) Vidal-Abarca, C.; Lavela, P.; Tirado, J. L. The Origin of Capacity Fading in $NiFe_2O_4$ Conversion Electrodes for Lithium Ion Batteries Unfolded by ^{57}Fe Mossbauer Spectroscopy. *J. Phys. Chem. C* **2010**, *114*, 12828–12832.
(22) Bomio, M.; Lavela, P.; Tirado, J. L. Electrochemical Evaluation of $CuFe_2O_4$ Samples obtained by Sol–Gel Methods used as Anodes in Lithium Batteries. *J. Solid State Electrochem.* **2008**, *12*, 729–737.
(23) Deng, Y.; Zhang, Q.; Tang, S.; Zhang, L.; Deng, S.; Shi, Z.; Chen, G. One-Pot Synthesis of $ZnFe_2O_4$/C Hollow Spheres as Superior Anode Materials for Lithium Ion Batteries. *Chem. Commun.* **2011**, *47*, 6828–6830.
(24) Sharma, Y.; Sharma, N.; Rao, G. V. S.; Chowdari, B. V. R. Li-Storage and Cyclability of Urea Combustion derived $ZnFe_2O_4$ as Anode for Li-Ion Batteries. *Electrochim. Acta* **2008**, *53*, 2380–2385.
(25) Guo, X.; Lu, X.; Fang, X.; Mao, Y.; Wang, Z.; Chen, L.; Xu, X.; Yang, H.; Liu, Y. Lithium Storage in Hollow Spherical $ZnFe_2O_4$ as Anode Materials for Lithium Ion Batteries. *Electrochem. Commun.* **2010**, *12*, 847–850.

(26) Sharma, Y.; Sharma, N.; Subba Rao, G. V.; Chowdari, B. V. R. Nanophase $ZnCo_2O_4$ as a High Performance Anode Material for Li-Ion Batteries. *Adv. Funct. Mater.* **2007**, *17*, 2855−2861.
(27) Poizot, P.; Laruelle, S.; Grugeon, S.; Dupont, L.; Tarascon, J. M. Searching for New Anode Materials for the Li-Ion Technology: Time to Deviate from the Usual Path. *J. Power Sources* **2001**, *97*−*98*, 235−239.
(28) Teh, P. F.; Pramana, S. S.; Sharma, Y.; Ko, Y. W.; Madhavi, S. Electrospun $Zn_{1-x}Mn_xFe_2O_4$ Nanofibers As Anodes for Lithium-Ion Batteries and the Impact of Mixed Transition Metallic Oxides on Battery Performance. *ACS Appl. Mater. Interfaces* **2013**, *5*, 5461−5467.
(29) Cherian, C.; Reddy, M. V.; Rao, G. V. S.; Sow, C.; Chowdari, B. V. R. Li-Cycling Properties of Nano-crystalline $(Ni_{1-x}Zn_x)Fe_2O_4$ ($0 \leq x \leq 1$). *J. Solid State Electrochem.* **2012**, *16*, 1823−1832.
(30) Manikandan, A.; Judith Vijaya, J.; Sundararajan, M.; Meganathan, C.; Kennedy, L. J.; Bououdina, M. Optical and Magnetic Properties of Mg-Doped $ZnFe_2O_4$ Nanoparticles Prepared By Rapid Microwave Combustion Method. *Superlattices Microstruct.* **2013**, *64*, 118−131.
(31) Vital, A.; Angermann, A.; Dittmann, R.; Graule, T.; Töpfer, J. Highly Sinter-Active (Mg−Cu)−Zn Ferrite Nanoparticles Prepared by Flame Spray Synthesis. *Acta Mater.* **2007**, *55*, 1955−1964.
(32) Bahiraei, H.; Shoushtari, M. Z.; Gheisari, K.; Ong, C. K. The Effect of Sintering Temperature on the Electromagnetic Properties of Nanocrystalline MgCuZn Ferrite Prepared by Sol−Gel Auto Combustion Method. *Mater. Lett.* **2014**, *122*, 129−132.
(33) Selvan, R. K.; Krishnan, V.; Augustin, C. O.; Bertagnolli, H.; Kim, C. S.; Gedanken, A. Investigations on the Structural, Morphological, Electrical, and Magnetic Properties of $CuFe_2O_4$−NiO Nanocomposites. *Chem. Mater.* **2007**, *20*, 429−439.
(34) Yao, L.; Hou, X.; Hu, S.; Wang, J.; Li, M.; Su, C.; Tade, M. O.; Shao, Z.; Liu, X. Green Synthesis of Mesoporous $ZnFe_2O_4$/C Composite Microspheres as Superior Anode Materials for Lithium-Ion Batteries. *J. Power Sources* **2014**, *258*, 305−313.
(35) Bresser, D.; Paillard, E.; Kloepsch, R.; Krueger, S.; Fiedler, M.; Schmitz, R.; Baither, D.; Winter, M.; Passerini, S. Carbon Coated $ZnFe_2O_4$ Nanoparticles for Advanced Lithium-Ion Anodes. *Adv. Energy Mater.* **2013**, *3*, 513−523.
(36) Martinez-Julian, F.; Guerrero, A.; Haro, M.; Bisquert, J.; Bresser, D.; Paillard, E.; Passerini, S.; Garcia-Belmonte, G. Probing Lithiation Kinetics of Carbon-Coated $ZnFe_2O_4$ Nanoparticle Battery Anodes. *J. Phys. Chem. C* **2014**, *118*, 6069−6076.
(37) NuLi, Y.-N.; Chu, Y.-Q.; Qin, Q.-Z. Nanocrystalline $ZnFe_2O_4$ and Ag-Doped $ZnFe_2O_4$ Films Used as New Anode Materials for Li-Ion Batteries. *J. Electrochem. Soc.* **2004**, *151*, A1077−A1083.
(38) Xia, H.; Qian, Y.; Fu, Y.; Wang, X. Graphene Anchored with $ZnFe_2O_4$ Nanoparticles as a High-Capacity Anode Material for Lithium-Ion Batteries. *Solid State Sci.* **2013**, *17*, 67−71.
(39) Xie, J.; Song, W.; Cao, G.; Zhu, T.; Zhao, X.; Zhang, S. One-Pot Synthesis of Ultrafine $ZnFe_2O_4$ Nanocrystals Anchored on Graphene for High-Performance Li and Li-Ion Batteries. *RSC Adv.* **2014**, *4*, 7703−7709.
(40) Zhang, G.; Yu, L.; Wu, H. B.; Hoster, H. E.; Lou, X. W. Formation of $ZnMn_2O_4$ Ball-in-Ball Hollow Microspheres as a High-Performance Anode for Lithium-Ion Batteries. *Adv. Mater.* **2012**, *24*, 4609−4613.
(41) Zhou, G.; Wang, D.-W.; Li, F.; Zhang, L.; Li, N.; Wu, Z.-S.; Wen, L.; Lu, G. Q.; Cheng, H.-M. Graphene-Wrapped Fe_3O_4 Anode Material with Improved Reversible Capacity and Cyclic Stability for Lithium Ion Batteries. *Chem. Mater.* **2010**, *22*, 5306−5313.
(42) Reddy, M. V.; Subba Rao, G. V.; Chowdari, B. V. R. Preparation and Characterization of $LiNi_{0.5}Co_{0.5}O_2$ and $LiNi_{0.5}Co_{0.4}Al_{0.1}O_2$ by Molten Salt Synthesis for Li Ion Batteries. *J. Phys. Chem. C* **2007**, *111*, 11712−11720.
(43) Reddy, M. V.; Wei Wen, B. L.; Loh, K. P.; Chowdari, B. V. R. Energy Storage Studies on $InVO_4$ as High Performance Anode Material for Li-Ion Batteries. *ACS Appl. Mater. Interfaces* **2013**, *5*, 7777−7785.
(44) Reddy, M. V.; Prithvi, G.; Loh, K. P.; Chowdari, B. V. R. Li Storage and Impedance Spectroscopy Studies on Co_3O_4, CoO, and CoN for Li-Ion Batteries. *ACS Appl. Mater. Interfaces* **2013**, *6*, 680−690.
(45) Reddy, M. V.; Madhavi, S.; Subba Rao, G. V.; Chowdari, B. V. R. Metal Oxyfluorides $TiOF_2$ and NbO_2F as Anodes for Li-Ion Batteries. *J. Power Sources* **2006**, *162*, 1312−1321.